Optics Letters

# High-Q chaotic lithium niobate microdisk cavity

Li Wang,[1,†] Cheng Wang,[2,†] Jie Wang,[3] Fang Bo,[3,5] Mian Zhang,[2] Qihuang Gong,[1,4] Marko Lončar,[2,6] and Yun-Feng Xiao[1,4,7]

[1]State Key Laboratory for Mesoscopic Physics and School of Physics, Peking University, Collaborative Innovation Center of Quantum Matter, Beijing 100871, China
[2]John A. Paulson School of Engineering and Applied Sciences, Harvard University, 29 Oxford Street, Cambridge, Massachusetts 02138, USA
[3]The MOE Key Laboratory of Weak Light Nonlinear Photonics, TEDA Applied Physics Institute and School of Physics, Nankai University, Tianjin 300457, China
[4]Collaborative Innovation Center of Extreme Optics, Shanxi University, Taiyuan 030006, Shanxi, China
[5]e-mail: fangbo@nankai.edu.cn
[6]e-mail: loncar@seas.harvard.edu
[7]e-mail: yfxiao@pku.edu.cn

Received 27 February 2018; revised 8 May 2018; accepted 12 May 2018; posted 18 May 2018 (Doc. ID 322691); published 13 June 2018

**Lithium niobate (LN) is the workhorse for modern optoelectronics industry and nonlinear optics. High quality ($Q$) factor LN microresonators are promising candidates for applications in optical communications, quantum photonics, and sensing. However, the phase-matching requirement of traditional evanescent coupling methods poses significant challenges to achieve high coupling efficiencies of the pump and signal light simultaneously, ultimately limiting the practical usefulness of these high $Q$ factor LN resonators. Here, for the first time, to the best of our knowledge, we demonstrate deformed chaotic LN microcavities that feature directional emission patterns and high $Q$ factors simultaneously. The chaotic LN microdisks are created using conventional semiconductor fabrication processes, with measured $Q$ factors exceeding $10^6$ in the telecommunication band. We show that our devices can be free-space-coupled with high efficiency by leveraging directional emission from the asymmetric cavity. Using this broadband approach, we demonstrate a 58-fold enhancement of free-space collection efficiency of a second harmonic generation signal, compared with a circular microdisk.** 

***OCIS codes:*** (140.3945) Microcavities; (130.3730) Lithium niobate; (230.5750) Resonators.

https://doi.org/10.1364/OL.43.002917

Single-crystal lithium niobate ($LiNbO_3$, LN) [1] is an important material for optical communications and various linear and nonlinear optical applications, thanks to its high second-order susceptibilities [$\chi^{(2)}$], wide transmission window, and relatively high ordinary and extraordinary refractive indices ($n_o = 2.21$, $n_e = 2.14$). Its nonlinear coefficients for second-harmonic generation (SHG, $d_{33} = 41.7$ pm/V) and electro-optic modulation ($r_{33} = 30.9$ pm/V) are high, compared with other commonly used $\chi^{(2)}$ materials. Microresonators, which manifest excellent light confinement in a small volume for a long time via total internal reflection, can greatly enhance the interaction between light and matter [2–4]. Combining the excellent physical properties of LN and the tremendous light field enhancement in microresonators, many demonstrations on high-$Q$ LN microresonators have recently been reported, showing great promise for efficient nonlinear optical processes on chip [5–16]. However, such systems typically suffer from a small coupling bandwidth due to the momentum mismatch between the resonator and the coupling fiber or prism [17–19], while the pump and signal wavelength in nonlinear processes are often dramatically different [20]. This key obstacle has become a major limitation for these high-$Q$ factor LN resonators.

In this Letter, we design a chaotic LN microcavity that supports high-$Q$ factor and directional emission at the same time, allowing for significantly more efficient coupling of pump and signal light in SHG process simultaneously. The deformed microdisk is fabricated by standard semiconductor fabrication process, which features $Q$ factors exceeding $10^6$ and supports efficient free-space coupling. The property of directional emission is verified by measuring the free-space coupling efficiency with different coupling angles. Using the deformed LN microcavity, we show nearly two orders of magnitude enhancement in SHG collection efficiency, compared with a circular LN cavity.

The geometric profile of the deformed microcavities is defined by an angle-dependent radius, $R(\phi) = R_0\sum_n[1 + a_n(\cos\phi)^n]$, where $\phi$ represents the polar angle, $R_0$ is a size parameter, and $a_n$ are shape parameters with fixed numbers ($a_2 = -0.0045$, $a_3 = -0.0305$, $a_4 = -0.0273$, $a_5 = 0.0314$, and $a_6 = -0.0381$).

The deformed microdisk resonators are fabricated on an LN-silica-silicon wafer prepared using ion slicing and wafer bonding techniques (NANOLN). The thicknesses of the LN device layer (z-cut), the sacrificial silica layer, and the silicon substrate are 0.5, 2, and 500 μm, respectively. The fabrication processes [21] are schematically illustrated in Fig. 1(a), which involves six major steps: UV-lithography, $Ar^+$ plasma etching, first HF etching, $XeF_2$ etching, and second HF etching. First,

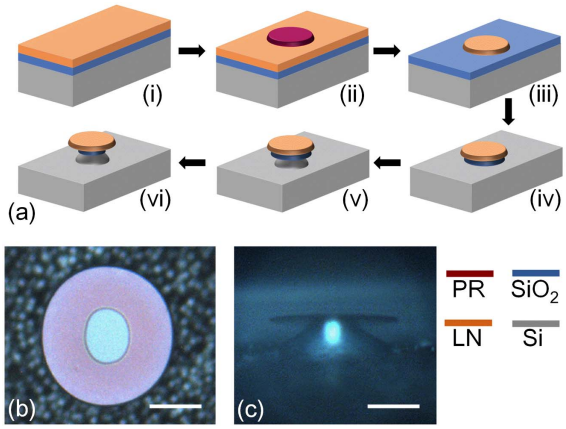


**Fig. 1.** (a) Fabrication processes: (i) LN thin film, (ii) UV-lithography, (iii) $Ar^+$ plasma etching, (iv) first HF wet etching, (v) $XeF_2$ dry etching, and (vi) second HF etching. (b) and (c) Optical microscope images of the deformed microdisk. Scale bar: 40 μm.

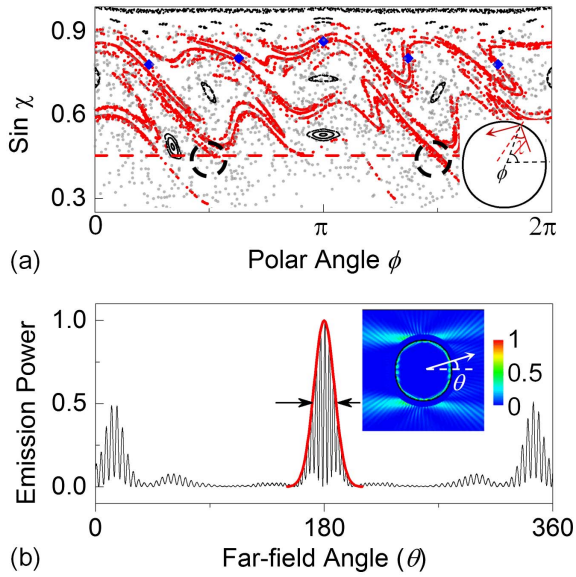


**Fig. 2.** (a) Poincaré surface of a section for internal ray dynamics with the Birkhoff coordinates sin $\chi$ and $\phi$, where $\chi$ and $\phi$ are defined in the inset. The red dashed line denotes the critical angle of refraction defined as $\sin\chi = 1/n$. The red dots represent the manifolds of the period-5 orbits (blue diamonds). The escaping points of the rays are indicated by black dashed circles. (b) Far-field emission pattern for the fundamental WGM calculated by wave simulation. The black arrows mark the FWHM of the main peak (enveloped by the red curve). Inset: the intracavity and near-field distribution of the mode. The power outside the cavity ($>1.1R$) is magnified by $10^5$ times.

a layer of photoresist (S1818, red layer) is prepared on the LN sample by a spin-coating method and patterned by UV-lithography. The designed deformed disk shape is transferred from a photomask prepared by electron beam lithography to the photoresist pads on top of the LN sample. Then the LN device layer (orange layer) is etched by $Ar^+$ plasma in a reactive ion beam etching system. The photoresist serves as the etching mask and ratio of the etching rate of the LN film, and the photoresist is about 1∶4. With a thickness of ∼2.5 μm, the photoresist pads protect the LN film underneath well during the entire plasma etching process. The finely polished top surface of the LN film is maintained, while the exposed part of a 500 nm thick LN layer is totally removed by the $Ar^+$ plasma. After the residual photoresist is removed using acetone, buffered HF is employed to undercut the silica layer (blue layer) from the edge of the LN disk. The etch rate of LN in buffered HF is very slow, which does not affect the roughness of the disk. Then $XeF_2$ gas is utilized to etch the silicon substrate (grey layer) and form the supporting pillar. Finally, a second HF wet etching is used to remove the silica layer remaining underneath the LN disk, except for the pillar region in the middle. We find that our fabrication process is capable of transferring our designed disk shape to the final device with high fidelity, thus ensuring the realization of chaos-assisted coupling.

The optical microscope images of a typical fabricated deformed microdisk are shown in Figs. 1(b) and 1(c), with an $R_0$ of 50 μm. The boundary shape of the deformed microdisk is in good agreement with the design. The brighter part in the center reveals the area of the silicon pillar. The inner black circle corresponds to the edge of the silica layer. In the side view image [Fig. 1(c)], the LN disk is more than 20 μm higher than the remaining silicon substrate, avoiding light leaking into the substrate when coupling with a free-space beam.

We use the Poincaré surface of section (SOS) to illustrate the ray dynamics of light in the designed microdisk profile [Fig. 2(a)] [22–28]. Here the Birkhoff coordinates sin $\chi$ and $\phi$ are used, where $\chi$ denotes the incident angle and $\phi$ the angular position of a reflection point of a random ray [inset of Fig. 2(a)] [28]. The SOS provides an intuitive picture of the angular momentum (sin $\chi$) of light when traveling at different locations of the resonator. In the SOS, ray trajectories are mostly chaotic (gray dots), except for some regular structures (black dots), including islands and Kolmogorov–Arnold–Moser curves. In ray dynamic theory, these two kinds of structures are disjointed with each other. However, in wave optics, the high-$Q$ whispering gallery modes (WGMs) located in the top regular structures can interact with the chaotic modes inside the chaotic sea through dynamical tunneling. Subsequently, the chaotic rays would converge to the manifolds of period-5 unstable orbits (blue diamonds) [20,23]. They decline along the manifolds (red dots) rapidly in the SOS until reaching the internal refractive critical line (red dashed line) and being refracted outside the cavity. With proper design of the cavity boundary, the escape events mainly occur around the two crossing points at $\phi \sim \pi/2$ and $3\pi/2$ (marked by black dashed circle). It is noted that Fig. 2(a) only displays rays with positive sin $\chi$, corresponding to counterclockwise modes. In comparison, for a circular microdisk cavity, the SOS only contains straight lines that correspond to WGM modes [23].

The far-field emission pattern of the fundamental WGM is numerically simulated by the boundary element method [Fig. 2(b)] [29,30]. There are three emission peaks. The main one (red curve) at a far-field angle $\theta \sim 180°$ corresponds to the escaping point around $\phi \sim \pi/2$ in Fig. 2(a). The peak has a full width at half-maximum (FWHM) of ∼19°, labeled by the red Gaussian envelope in Fig. 2(b). One of the secondary peaks at $\theta \sim 0°$ corresponds to the escaping point around $\phi \sim 3\pi/2$. The other secondary peak corresponds to the escaping point of the clockwise mode which is not shown in Fig. 2(a). Note that the wave simulation result has some differences with

the ray dynamics prediction and is more accurate. The inset of Fig. 2(b) shows the intracavity and near-field power distribution of the fundamental mode. The field intensity outside the cavity is magnified by $10^5$ times, compared with the intracavity intensity to illustrate the emission direction. Emission along far-field directions $\theta \sim 180°$ and 0° can be clearly seen, corresponding to cavity boundary angles $\phi \sim \pi/2$ and $3\pi/2$, respectively. In addition, the simulated $Q$ factor of the fundamental mode in this deformed microcavity with a small $R_0 \sim 11$ μm exceeds $10^7$ (limited by radiation loss).

The deformed LN microdisks are characterized in the telecommunication wavelength (~1550 nm) band by utilizing a free-space optical coupling system. The probe laser is launched from a tunable diode laser source (TLB-6328, New Focus), which then passes through a polarization controller and a fiber collimator. A long-working-distance objective lens focuses the probe beam onto the edge of the deformed microdisk from 180° far-field direction, which is the reverse of the preferential emission direction. The diameter of the waist of the focusing beam is about 3 μm. Another objective lens is used to collect the transmitted light in the 0° far-field direction. The collected light is measured by a photoreceiver (Newport, 1811-FC) connected to an oscilloscope (YOKOGAWA, DLM2034). We place the LN sample on a three-dimensional translation stage which can be rotated to focus the pump laser on different positions of the cavity periphery.

By scanning the probe laser wavelength, a transmission spectrum from 1545 to 1555 nm of the free-space-coupled deformed microdisk can be obtained [Fig. 3(a)]. Compared with the typical transmission spectra obtained from fiber-taper-coupled circular microcavities [5–11], many more modes with different linewidths are observed here. Due to the dynamic tunneling, from neighboring chaotic orbits to WGM-like orbits, a strict phase-matching condition for coupling is no longer needed. In the free-space beam-coupled transmission spectrum, most modes show Fano-like line shapes instead of standard Lorentzian line shapes, because of the strong interference between different modes [27,31]. Figure 3(b) shows zoom-in views of spectral ranges I and II indicated by the gray shadows in Fig. 3(a). The modes belonging to the same mode families are indicated by shadows with the same color. The free spectral ranges (FSRs) of the mode families A and B are ~4.3 nm, which agrees well with the numerical simulation result of an LN resonator with the actual device dimensions. The modes I-A and II-A [Fig. 3(c)] are efficiently excited with $Q$ factors on the order of $10^5$. The high-$Q$ mode II-B around 1551.4 nm [Fig. 3(c)] is fitted by the Lorentzian line shape (red curve). The $Q$ factor is found to be $1.5 \times 10^6$, which is mainly limited by surface scattering.

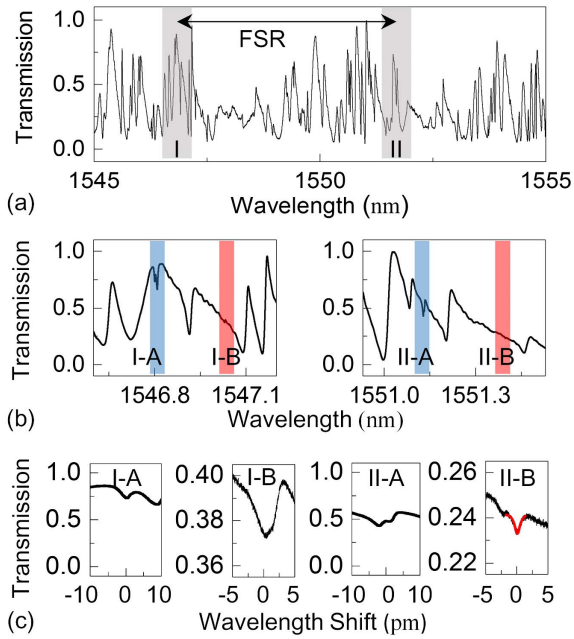


**Fig. 3.** (a) Transmission spectrum of a deformed microdisk with $R_0 \sim 50$ μm coupled by a free-space optical coupling system. (b) Zoom-in views of spectral ranges I and II [gray shadows in (a)], separated by the FSR. (c) Zoom-in views of the modes marked by shadows in (b). Modes A and B belong to two different mode families, indicated by blue and red, respectively. Mode II-B in (c) is fitted using the Lorentzian function, showing a $Q$ factor ~$10^6$.

To further study the emission property of the deformed LN microdisk, we couple the free-space beam to the microdisk at different coupling angles $\varphi$. Thanks to the reciprocity of light, the primary emission direction is also the easiest direction for the probe light to couple in. As the inverse process of directional emission, the rays first refract into the SOS near the critical line, then diffuse into the upper chaotic region and, finally, excite the high-$Q$ WGMs through dynamical tunneling. We record the transmission dip values (left inset of Fig. 4), which approximately characterize the coupling efficiency [32], of the target mode with $Q \sim 10^6$ for different coupling angles $\varphi$. It is found that the coupling efficiency strongly depends on the coupling angle (Fig. 4). At $\varphi \sim 0°$ and 180°, the dip value approaches the maximum. The coupling efficiencies at other $\varphi$ values are much lower. There is no observable high-$Q$ mode in the transmission spectrum when $\varphi$ varies around 90° and 270°. This agrees well with the theoretical design in which the highly directional emissions are mainly along $\theta \sim 0°$ and 180° ($\phi \sim \pi/2$ and $3\pi/2$). Considering the whole coupling process including both excitation and collection, the obtained dip values of $\varphi \sim 0°$ and 180° are similar.

Figure 5 shows that SHG signals can be much more efficiently collected using the deformed microcavity, compared with a circular microdisk. We use a spectrometer (DU971N-UV, Andor) to monitor the output SHG signal near 775 nm while pumping at ~1550 nm. Under the same pump power ~5 mW, the free-space-coupled SHG signal power from the

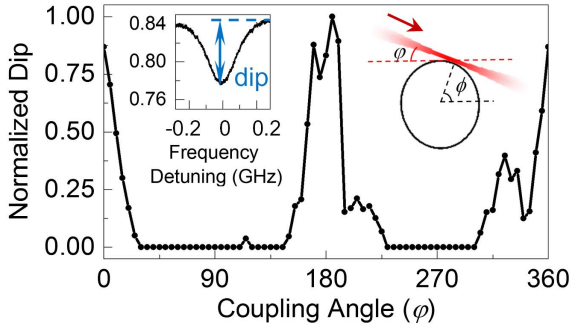


**Fig. 4.** Normalized dip versus coupling angle. The left inset shows the target mode ($Q \sim 10^6$) and the definition of the dip. The right inset defines the coupling angle $\varphi$.

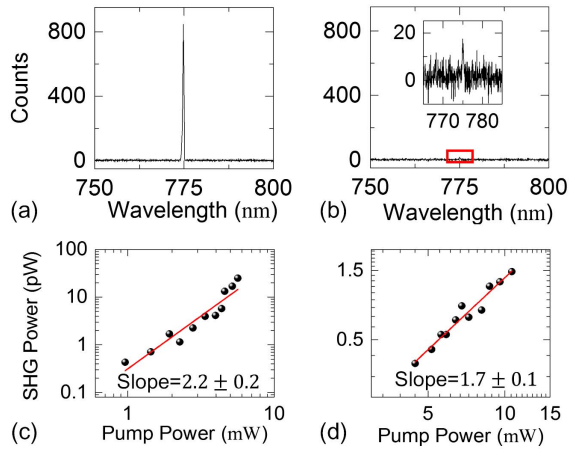


**Fig. 5.** (a) and (b) Spectrometer data showing the SHG signals of a deformed microcavity (a) and a circular microcavity (b) under the same pump power. (c) and (d) SHG input–output power relations in the deformed (c) and circular (d) microcavities. The inset shows the weak signal marked by the red square in (b).

deformed microdisk [Fig. 5(a)] is 58 times larger than that from the circular microdisk [Fig. 5(b)]. Figures 5(c) and 5(d) show the input–output power relations in logarithmic scale for both cases, measured by the spectrometer. The fitted slopes of the deformed and circular cavities are $2.2 \pm 0.2$ [Fig. 5(c)] and $1.7 \pm 0.1$ [Fig. 5(d)], which is in agreement with the property of second-order nonlinear process. Note we did not optimize the phase matching of the nonlinear process; therefore, the overall conversion efficiency is relatively low currently. Combining phase-matching techniques with our deformed cavities, simultaneously high conversion and collection efficiencies can be achieved in the future.

In summary, we have designed and characterized a deformed LN microcavity which simultaneously supports high-$Q$ factor and directional emission properties. We measure $Q$ factors exceeding $10^6$ and realize efficient free-space coupling. The cavity coupling strength is strongly dependent on the coupling angle of free-space beam, which leads to a 58-time enhancement of the collected SHG power, compared with a circular microdisk.

**Funding.** The National Key R&D Program of China (2016YFA0301302); National Natural Science Foundation of China (NSFC) (11474011, 11654003, 61435001, 61611540346, 11674181, 11734009); National Science Foundation (NSF) (ECCS-1609549, ECCS-1740296 E2CDA).

**Acknowledgment.** The authors thank Linbo Shao, Shu-Xin Zhang, and Zhenzhong Hao for fruitful discussions. L. Wang and Y.-F. Xiao were supported by High-performance Computing Platform of Peking University. C. Wang, M. Zhang, and M. Lončar were supported by NSF, Harvard University Office of Technology Development (Physical Sciences and Engineering Accelerator Award).

[†]These authors contributed equally to this work.

## REFERENCES

1. D. N. Nikogosyan, *Nonlinear Optical Crystals: A Complete Survey* (Springer, 2005).
2. K. J. Vahala, Nature **424**, 839 (2003).
3. J. Ward and O. Benson, Laser Photon. Rev. **5**, 553 (2011).
4. A. B. Matsko and V. S. Ilchenko, IEEE J. Sel. Top. Quantum Electron. **12**, 3 (2006).
5. T.-J. Wang, J.-Y. He, C.-A. Lee, and H. Niu, Opt. Express **20**, 28119 (2012).
6. C. Wang, M. J. Burek, Z. Lin, H. A. Atikian, V. Venkataraman, I. C. Huang, P. Stark, and M. Lončar, Opt. Express **22**, 30924 (2014).
7. R. Wang and S. A. Bhave, "Free-standing high quality factor thin-film lithium niobate micro-photonic disk resonators," arXiv:1409.6351 (2014).
8. J. Lin, Y. Xu, Z. Fang, M. Wang, J. Song, N. Wang, L. Qiao, W. Fang, and Y. Cheng, Sci. Rep. **5**, 8072 (2015).
9. J. Lin, Y. Xu, Z. Fang, M. Wang, N. Wang, L. Qiao, W. Fang, and Y. Cheng, Sci. China: Phys. Mech. Astron. **58**, 114209 (2015).
10. J. Wang, F. Bo, S. Wan, W. Li, F. Gao, J. Li, G. Zhang, and J. Xu, Opt. Express **23**, 23072 (2015).
11. M. Zhang, C. Wang, R. Cheng, A. Shams-Ansari, and M. Lončar, Optica **4**, 1536 (2017).
12. L. Chen, Q. Xu, M. G. Wood, and R. M. Reano, Optica **1**, 112 (2014).
13. C. Wang, M. Zhang, B. Stern, M. Lipson, and M. Lončar, Opt. Express **26**, 1547 (2018).
14. R. Luo, H. Jiang, H. Liang, Y. Chen, and Q. Lin, Opt. Lett. **42**, 1281 (2017).
15. R. Luo, H. Jiang, S. Rogers, H. Liang, Y. He, and Q. Lin, Opt. Express **25**, 24531 (2017).
16. J. T. Lin, Y. X. Xu, J. L. Ni, M. Wang, Z. W. Fang, L. L. Qiao, W. Fang, and Y. Cheng, Phys. Rev. Appl. **6**, 014002 (2016).
17. J. C. Knight, G. Cheung, F. Jacques, and T. A. Birks, Opt. Lett. **22**, 1129 (1997).
18. M. Cai, O. Painter, and K. J. Vahala, Phys. Rev. Lett. **85**, 74 (2000).
19. G. Liu, V. S. Iichenko, T. Su, Y.-C. Ling, S. Feng, K. Shang, Y. Zhang, W. Liang, A. A. Savchenkov, A. B. Matsko, L. Maleki, and S. J. Ben Yoo, Optica **5**, 219 (2018).
20. X. Jiang, L. Shao, S.-X. Zhang, X. Yi, J. Wiersig, L. Wang, Q. Gong, M. Lončar, L. Yang, and Y.-F. Xiao, Science **358**, 344 (2017).
21. G. Ulliac, V. Calero, A. Ndao, F. I. Baida, and M.-P. Bernal, Opt. Mater. **53**, 1 (2016).
22. H. G. Schwefel, N. B. Rex, H. E. Tureci, R. K. Chang, A. D. Stone, T. Ben-Messaoud, and J. Zyss, J. Opt. Soc. Am. B **21**, 923 (2004).
23. J. Wiersig and M. Hentschel, Phys. Rev. Lett. **100**, 033901 (2008).
24. S. Shinohara, T. Harayama, T. Fukushima, M. Hentschel, T. Sasaki, and E. E. Narimanov, Phys. Rev. Lett. **104**, 163902 (2010).
25. Q. H. Song, L. Ge, A. D. Stone, H. Cao, J. Wiersig, J.-B. Shim, J. Unterhinninghofen, W. Fang, and G. S. Solomon, Phys. Rev. Lett. **105**, 103902 (2010).
26. Z.-X. Xiao, Y.-Z. Huang, Y.-D. Yang, J.-L. Xiao, and X.-W. Ma, Opt. Lett. **42**, 1309 (2017).
27. Q.-F. Yang, X.-F. Jiang, Y.-L. Cui, L. Shao, and Y.-F. Xiao, Phys. Rev. A **88**, 023810 (2013).
28. H. Cao and J. Wiersig, Rev. Mod. Phys. **87**, 61 (2015).
29. J. Wiersig, J. Opt. A **5**, 53 (2003).
30. C.-L. Zou, Y. Yang, Y.-F. Xiao, C.-H. Dong, Z.-F. Han, and G.-C. Guo, J. Opt. Soc. Am. B **26**, 2050 (2009).
31. Y.-F. Xiao, X.-F. Jiang, Q.-F. Yang, L. Wang, K. Shi, Y. Li, and Q. Gong, Laser Photon. Rev. **7**, L51 (2013).
32. S.-X. Zhang, L. Wang, Z.-Y. Li, Y. Li, Q. Gong, and Y.-F. Xiao, Opt. Lett. **41**, 4437 (2016).